

JGR Space Physics

RESEARCH ARTICLE

10.1029/2020JA029071

Key Points:

- The global ionospheric low-frequency response to a sequence of recurrent structures in the solar wind is analyzed using ionosonde data
- The ionospheric NmF₂ and hmF₂ spectra indicate that nonlinear interactions transfer power from the main spectral peaks to secondary ones
- The ionospheric spectra correlate best with the solar wind magnetic field B_z and geomagnetic index SYM-H

Correspondence to:

C. Negrea,
negreacatalin@spacescience.ro

Citation:

Negrea, C., Munteanu, C., & Echim, M. M. (2021). Global ionospheric response to a periodic sequence of HSS/CIR events during the 2007–2008 solar minimum. *Journal of Geophysical Research: Space Physics*, 126, e2020JA029071. <https://doi.org/10.1029/2020JA029071>

Received 6 JAN 2021

Accepted 23 APR 2021

© 2021. American Geophysical Union.
 All Rights Reserved.

Global Ionospheric Response to a Periodic Sequence of HSS/CIR Events During the 2007–2008 Solar Minimum

C. Negrea¹ , C. Munteanu² , and M. M. Echim^{1,2} 

¹Institute of Space Science, Magurele, Romania, ²Belgian Institute for Space Aeronomy, Brussels, Belgium

Abstract In this study, we investigate the global ionospheric impact of high-speed solar wind streams/corotating interaction regions (HSS/CIR). A series of 10 such events are identified between December 1, 2007 and April 29, 2008, characterized in the frequency domain by the main spectral peaks corresponding to 27, 13.5, 9, and 6.75 days. The spectra of solar wind magnetic field, speed, and proton density, as well as those of the geomagnetic indices AE and SYM-H, are solely dominated by these features. By contrast, the ionospheric NmF₂ and to a lesser extent the hmF₂ spectra have a much more complex structure, with secondary peaks adding to or replacing the main ones. We argue that this is evidence of the nonlinear nature of the magnetosphere-ionosphere coupling, highlighted particularly in the NmF₂ ionospheric response. Additionally, we show that hmF₂ is more closely correlated than NmF₂ to all parameters describing the solar wind and geomagnetic activity. Finally, the ionospheric response shows a higher correlation with B_z than any other solar wind parameter, and higher with SYM-H than AE, indicating that for the low-frequency part of the spectrum, high-latitude Joule heating and particle precipitation play a secondary role to that of prompt penetration electric fields in dictating the ionospheric response to geomagnetic activity, in the case of this sequence of HSS/CIR events.

1. Introduction

The thermosphere-ionosphere system constitutes the upper-most layer of the Earth's atmosphere and is characterized by high variability and a strong dependence on external drivers. The two main categories of forcings are solar radiation and geomagnetic activity at high latitudes. Under normal conditions, solar radiation is the dominant source of energy and momentum, generating the standard structure, composition, and circulation of the thermosphere-ionosphere (Fuller-Rowell, 2014; Rishbeth & Garriott, 1969). During geomagnetic storms, the energy input at high latitudes can be significant, or even dominant. During such events, there is an increase of particle precipitation and Joule heating (Codrescu et al., 1995) at high latitudes, together with penetration electric fields at mid- and low-latitudes. The resulting plasma drift and associated ion-drag will heat up the neutral atmosphere, inducing pressure gradients that can alter the global neutral circulation from a dayside-nightside pattern of winds to an equatorward pattern. Additionally, since the Joule heating maximum occurs around 100–120 km altitude, the heavier molecular species dominant here (molecular oxygen and molecular nitrogen) will be displaced toward higher altitudes, while the atomic oxygen density will decrease due to equatorward winds (Fuller-Rowell et al., 1994). The resulting modified chemical composition will in turn lead to a higher plasma loss rate through charge exchange and recombination, as well as a decrease in plasma production due to the loss of atomic oxygen.

The occurrence of geomagnetic storms is linked to solar activity and transient events in the solar wind. During the descending and minimum phases of a solar cycle, the near-Earth solar wind is dominated by high-speed streams (HSSs) and their associated stream interaction regions (SIRs), characterized by increased plasma density and magnetic field intensity. These structures are formed when the fast-solar wind emanating from a solar coronal hole (CH) “collides” with the slower solar wind ahead of it. Coronal holes lasting for several solar rotations will generate recurring SIRs, also known as corotating interaction regions (CIRs). The ionospheric impact of geomagnetic storms and of HSS/CIR sequences is an active area of research, with multiple recent studies employing a variety of data types and approaches: TEC (Chen et al., 2015; Verkhoglyadova, Tsurutani, Mannucci, Mlynczak, Hunt, Komjathy, & Runge, 2011; Verkhoglyadova, Tsurutani, Mannucci, Mlynczak, Hunt, & Runge, 2013), ionosonde data, primarily NmF₂ (Grandin et al., 2015; Wang et al., 2011), satellite measurements from CHAMP (McGranaghan et al., 2014; Xu et al., 2015), TIMED

(Crowley et al., 2008), COSMIC (Tulasi Ram, Lei, et al., 2010; Tulasi Ram, Liu, & Su, 2010), as well as modeling tools (Fuller-Rowell et al., 1994; Klenzing et al., 2013; Wang et al., 2011).

The early minimum phase of solar cycle 23 (2007–2008) was particularly dominated by the periodic recurrence of HSS/CIR events (Guo et al., 2012; Lei, Thayer, Wang, & McPherron, 2011; Tulasi Ram, Lei, et al., 2010). Munteanu, Hamada, and Mursula (2019) demonstrated the existence of two dominant sequences of HSS/CIR events recurring with similar properties over five solar rotations, from December 2007 to April 2008. They showed that each HSS/CIR event produced strong high-latitude activity (substorms) as observed in the AE index and a minor storm, as observed in the SYM-H index. The whole heliosphere interval (WHI) between March 20 and April 16, 2008 (Carrington rotation 2068) was part of an international campaign to study the solar-heliospheric-planetary system near the solar minimum between cycles 23 and 24 (Echer et al., 2011; Gibson, de Toma, et al., 2011; Gibson, Kozyra, et al., 2009; Maris & Maris, 2009; Thompson et al., 2011; Webb et al., 2011). Lei, Thayer, Wang, and McPherron (2011) showed that the HSSs/CIRs around the WHI interval were geoeffective both in terms of geomagnetic activity as well as thermospheric density response, with relative changes in neutral density due to HSSs/CIRs as large as 75%, which indicates that HSSs/CIRs have a significant impact on the variability of the thermosphere, even though the resultant geomagnetic activity is weak or moderate.

The recurring nature of the solar wind perturbations associated with HSS/CIRs induce recurring geomagnetic events characterized by periodicities of 27 days, as well as the higher harmonics at 13.5, 9, and 6.75 days (Crowley et al., 2008; Katsavrias et al., 2012; Lei, Thayer, Wang, & McPherron, 2011). Finally, the response of the thermosphere-ionosphere to these storms is characterized by the same periodicities (Emery et al., 2011; Lei, Thayer, Forbes, et al., 2008; Lei, Thayer, Wang, & McPherron, 2011; Pedatella et al., 2010; Tulasi Ram, Lei, et al., 2010; Tulasi Ram, Liu, & Su, 2010; Xu et al., 2015), as well as additional spectral peaks (Wang et al., 2011).

In this study, we aim to describe the global response of the ionosphere to the series of HSS/CIRs between December 2007 and April 2008. For this purpose, we used ionosonde NmF₂ and hmF₂ data from the NOAA-NCEI database (<http://ngdc.noaa.gov/ionosonde/data>), as well as complementary OMNI data sets (King & Papitashvili, 2005) for solar wind parameters and geomagnetic indices. We applied a spectral analysis method based on the Lomb-Scargle method to highlight dominant spectral features, while simultaneously taking into account the differences in sampling between the different data sets. To further account for differences caused by the geographical location and local conditions at each station, the spectra were individually normalized to 1, allowing for comparisons between results obtained at different locations. The results provide a comprehensive image of the global ionospheric response to the series of HSS/CIR events recorded in 2007–2008.

The paper is structured as follows: Section 1 contains the introduction, Section 2 describes the ionosonde NmF₂ and hmF₂ data, the OMNI solar wind measurements and geomagnetic indices, as well as the data processing and analysis methodology. Section 3 contains the main geophysical results and their discussion, and finally, Section 4 lists our conclusions.

2. Data Set and Analysis Methodology

The ionospheric response is studied using ionosonde NmF₂ and hmF₂ data publicly available through the National Oceanic and Atmospheric Administration–National Centers for Environmental Information (NOAA–NCEI) website. A total of 28 stations provided measurements for the period of interest (December 1, 2007–April 30, 2008), a complete list of which is given in Table 1. At all locations, a threshold of 2 was used as a filter for the quality figure automatically generated by QualScan (McNamara, 2006), excluding poor quality data. Additionally, subgroups of stations are highlighted using a color code: dark-blue for high-latitude stations, dark-orange for mid-latitude northern hemisphere stations, dark-red for low-latitude locations, and light-orange for the mid-latitude southern hemisphere. The data acquisition is performed independently at each location, and subject to different local conditions, such as magnetic latitude or weather patterns. This can potentially give rise to discrepancies in the dynamic range and sampling characterizing each station. A sample time series spanning 4 months of data from the RAL ionosonde is displayed in Figure 1, and it shows the impact of 10 geomagnetic storms caused by recurring CIR/HSS events, where

Table 1

List of Ionosonde Stations, Together With Geographic Latitude and Longitude, Start and End-Date for the Available Data, Typical Sampling Frequency and Percentage Data Coverage

| Station code | Latitude (°) | Longitude (°) | Start date | End date | Sampling frequency (min ⁻¹) | Data coverage (%) |
|--------------|--------------|---------------|-------------------|-----------------|---|-------------------|
| THJ77 | 77.5 | 290.8 | December 1, 2007 | April 29, 2008 | 15 5 | 73.7% |
| TR169 | 69.6 | 19.2 | December 17, 2007 | April 29, 2008 | 15 | 20.8% |
| SMJ67 | 66.98 | 309.06 | December 1, 2007 | April 29, 2008 | 15 5 | 31.3% |
| CO764 | 64.9 | 212 | December 1, 2007 | April 29, 2008 | 15 | 36.7% |
| GA762 | 62.38 | 215 | December 1, 2007 | April 29, 2008 | 15 | 15.6% |
| NQJ61 | 61.2 | 314.6 | December 1, 2007 | April 29, 2008 | 15 | 28.6% |
| KS759 | 58.4 | 203.6 | December 1, 2007 | April 29, 2008 | 15 | 47.2% |
| JR055 | 54.6 | 13.4 | December 1, 2007 | April 29, 2008 | 15 | 48.0% |
| GSJ53 | 53.3 | 299.7 | December 1, 2007 | April 29, 2008 | 15 | 25.6% |
| FF051 | 51.7 | 358.2 | December 1, 2007 | April 29, 2008 | 15 | 79.1% |
| RL052 | 51.6 | 358.7 | December 25, 2007 | April 29, 2008 | 10 | 62.7% |
| PQ052 | 50 | 14.5 | December 1, 2007 | April 29, 2008 | 15 | 62.3% |
| MHJ45 | 42.6 | 288.5 | December 1, 2007 | April 29, 2008 | 7.5 15 | 20.1% |
| RO041 | 41.9 | 12.5 | December 1, 2007 | April 29, 2008 | 15 | 58.2% |
| EB040 | 40.8 | 0.5 | December 1, 2007 | April 29, 2008 | 15 | 73.7% |
| BC840 | 40 | 255 | December 1, 2007 | April 29, 2008 | 15 | 60.4% |
| AT138 | 38 | 23.5 | December 1, 2007 | April 29, 2008 | 15 | 48.2% |
| WP937 | 37.9 | 284.5 | December 1, 2007 | January 7, 2008 | 15 | 20.2% |
| EA036 | 37.1 | 353.3 | December 1, 2007 | April 29, 2008 | 15 | 74.8% |
| PA836 | 34.7 | 239.4 | December 1, 2007 | April 29, 2008 | 15 | 64.2% |
| DS932 | 32.4 | 260.2 | December 1, 2007 | April 29, 2008 | 15 | 56.1% |
| KJ609 | 9 | 167.2 | December 1, 2007 | April 29, 2008 | 15 | 39.2% |
| AS00Q | -7.95 | 345.6 | December 1, 2007 | April 29, 2008 | 15 | 49.9% |
| JJ91J | -12 | 283.2 | December 1, 2007 | April 29, 2008 | 15 | 61.1% |
| MU12K | -22.4 | 30.9 | December 25, 2007 | April 29, 2008 | 30 | 41.7% |
| LV12P | -28.5 | 21.2 | December 25, 2007 | April 29, 2008 | 30 | 47.8% |
| GR13L | -33.3 | 26.5 | December 1, 2007 | April 29, 2008 | 15 | 73.4% |
| PSJ5J | -51.6 | 302.1 | December 26, 2007 | April 8, 2008 | 30 | 11.3% |

the areas shaded with red and blue denote the time periods associated with the two HSS/CIR sequences identified by Munteanu, Hamada, and Mursula (2019). Also, a 10-day long subset from the same location highlights the ionospheric response to two particular geomagnetic events, started around March 26, 2003 and April 4, 2008 in Figures 1b and 1d. The typical storm ionospheric response is seen, characterized by a sudden increase in density at the outset of the storm (the positive phase), followed by a decrease in density lasting several days (the negative phase). It should however be noted that the specific ionospheric response to geomagnetic events can be more complex, particularly for moderate events (Matamba et al., 2015), such as the ones investigated in this study.

In order to highlight the wide range of the natural ionospheric variability, as well as that of the response to geomagnetic storms, Figure 2 illustrates the data at Millstone Hill. The extent of the differences in seasonal variability can be glean by comparing Panels 1a,c with 2a,c, and the differences in ionospheric response is evident by comparing Panels 1b,d with 2b,d. For example, the beginning of the negative storm phase at Millstone Hill is a full day later than at RAL for the event commencing on March 25, 2008, while for the

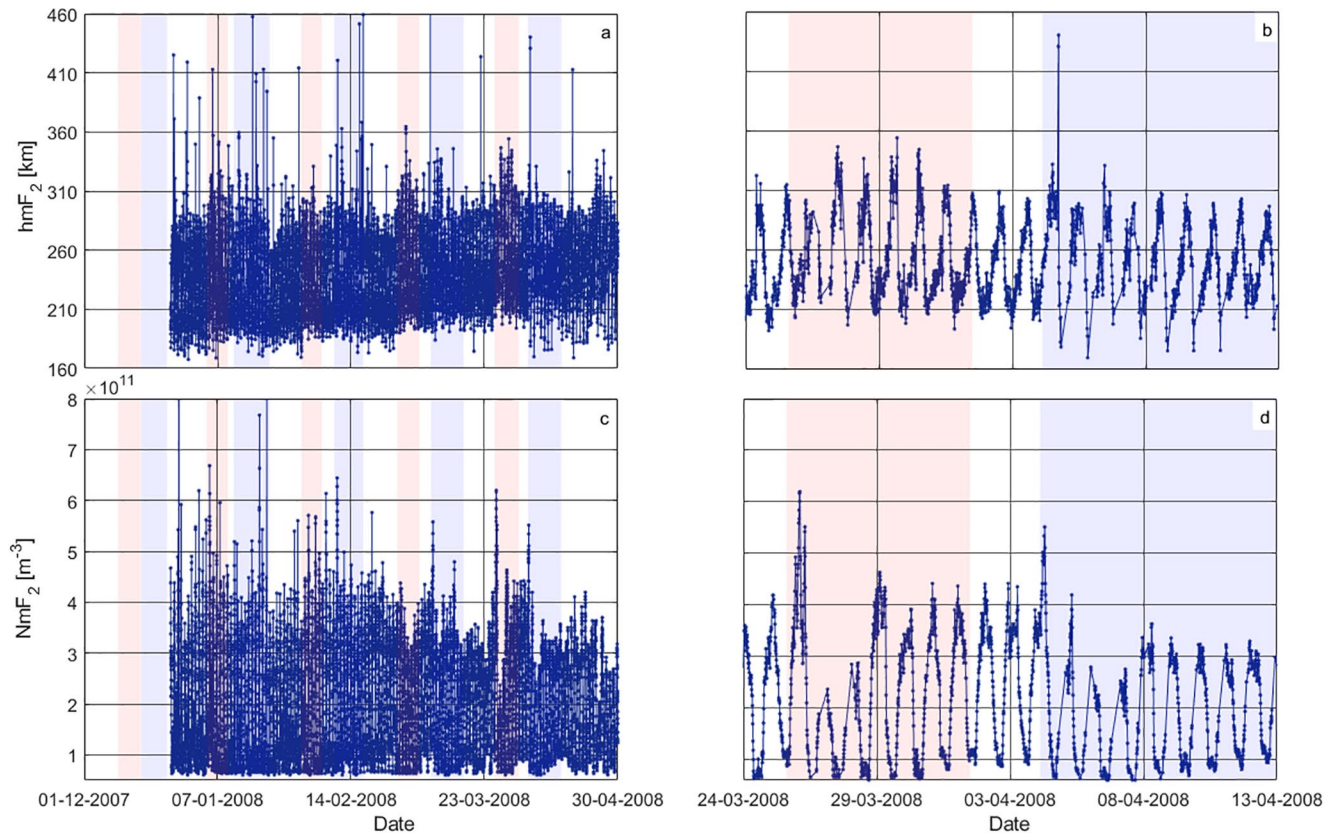


Figure 1. Sample data set from the RAL ionosonde (51.6°latitude, 358.7° longitude): (a) full hmF_2 data set, (b) 20-day long hmF_2 subsets showing the impact of two consecutive CIR events, (c) full NmF_2 data set and (d) same as Panel c, but for NmF_2 . The shaded areas delineate time periods associated with HSS/CIR events. CIR, corotating interaction regions; HSS, high-speed streams.

event commencing on April 4, 2008 the relative change in NmF_2 is larger during the positive storm phase at Millstone Hill, and larger at RAL during the negative phase.

The variations in solar wind velocity, density, magnetic field exhibit several periodicities linked to the interaction of these structures with the Earth’s magnetosphere and are subject of several studies (see e.g., Munteanu, Hamada, & Mursula, 2019). The magnetosphere itself reacts through a series of geomagnetic storms that follows in general the periodic trends of interplanetary driving. However, some notable differences are observed as discussed by Munteanu, Hamada, and Mursula (2019). They demonstrated that the Russell–McPherron (R–M) effect (Russell & McPherron, 1973) systematically increased (decreased) the geoeffectiveness of the negative (positive) polarity HSS/CIR streams. The R–M effect did not significantly affect the intensity of the storms caused by the R–M geoeffective streams but rather increased the duration of their main phases by up to 3 days. Thus, the ionosphere is subject to two types of forces, (a) the interplanetary forcing characterized by “pure” periodicities exhibited by solar wind parameters and (b) the geomagnetic/magnetospheric forcing characterized by recurrent/periodic occurrence of storms and substorms. A quantitative measure of the intensity of the magnetospheric forcing is given by geomagnetic indices like the auroral AE and equatorial SYM-H. A full set of parameters of interest is depicted in Figure 3.

The sampling of the ionosonde data is generally uniform for 25 stations, while at three locations it varies between two values. Also, the sampling rates can differ from station to station, as can be seen in Figures 1 and 2: at RAL the sampling rate is 1/10 min, while at Millstone Hill it oscillates between 1/7.5 min and 1/15 min. Additionally, this is different from the sampling rate of the solar wind measurements, which is 1/min. All data sets, except for the geomagnetic indices, contain data gaps of varying sizes and distributions. Table 1 lists for each station, the start and end date for which measurements were available, as well as the overall data coverage and sampling frequency. The percentages are smaller than those for the solar wind

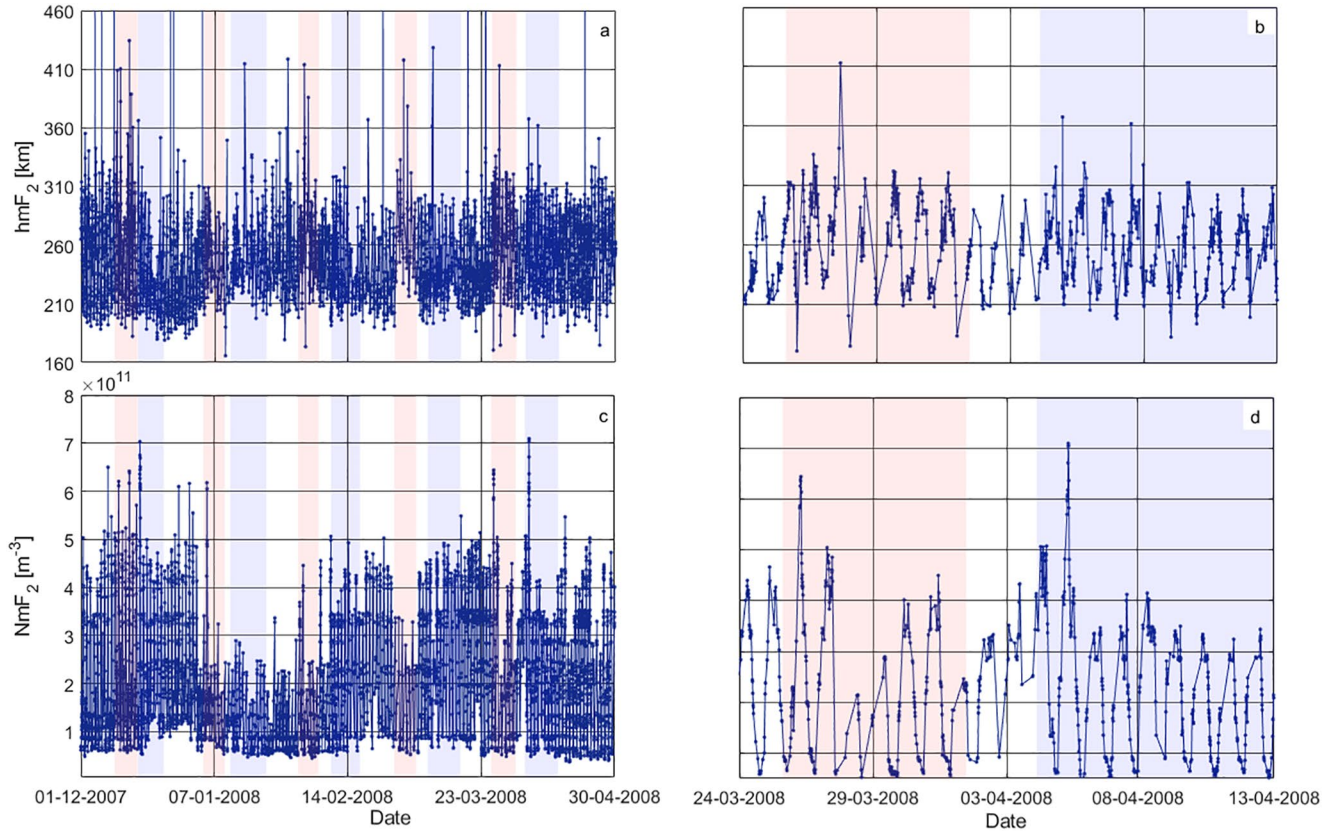


Figure 2. Same as Figure 1, but for the Millstone Hill (42.6° latitude, 288.5° longitude) ionosonde.

measurements, which are 95.35% for the magnetic field B_z component, 83.93% for solar wind speed, V , and 83.92% for the proton density (n_p).

In order to account for these differences and obtain comparable spectra, a Lomb-Scargle implementation is used (Lomb, 1976; Scargle, 1982), allowing for equivalent spectra to be obtained for all locations and measurement types, despite the different amounts of data available and the presence of data gaps (Munteanu, Negrea, et al., 2016). The amplitude spectra as a function of the period is defined as:

$$X(P) = \sqrt{\frac{2}{N} \left[\frac{\left(\sum_i (x_i - \bar{x}) \cos \omega(t_i - \tau) \right)^2}{\sum_i \cos^2 \omega(t_i - \tau)} + \frac{\left(\sum_i (x_i - \bar{x}) \sin \omega(t_i - \tau) \right)^2}{\sum_i \sin^2 \omega(t_i - \tau)} \right]} \quad (1)$$

with the parameters: $\bar{x} = \frac{1}{N} \sum_i x_i$, $\tan(2\omega\tau) = \frac{\sum_i \sin 2\omega t_i}{\sum_i \cos 2\omega t_i}$, $\omega = \frac{2\pi}{P}$ is the angular frequency, P is the period and N is the size of the data set (t_i, x_i). Figure 4 shows sample hmF_2 and NmF_2 spectra from the RAL ionosonde, covering the entire data set. For periods of a day or more, the extent of the data gaps is unlikely to affect our results. The impact of several sources of variability can be seen: at periods of several hours or less, the spectrum reflects the impact of small-scale structures, predominantly gravity-wave (GW) induced traveling ionospheric disturbances (TIDs). Some of these disturbances are likely connected to geomagnetic activity, being either large scale TIDs (Borries et al., 2009) or part of the background level of ionospheric disturbances (Negrea, Zobotin, & Bullett, 2018; Negrea, Zobotin, Bullett, Fuller-Rowell, et al., 2016). Superimposed are several dominant spectral peaks corresponding to the diurnal variation and its harmonics

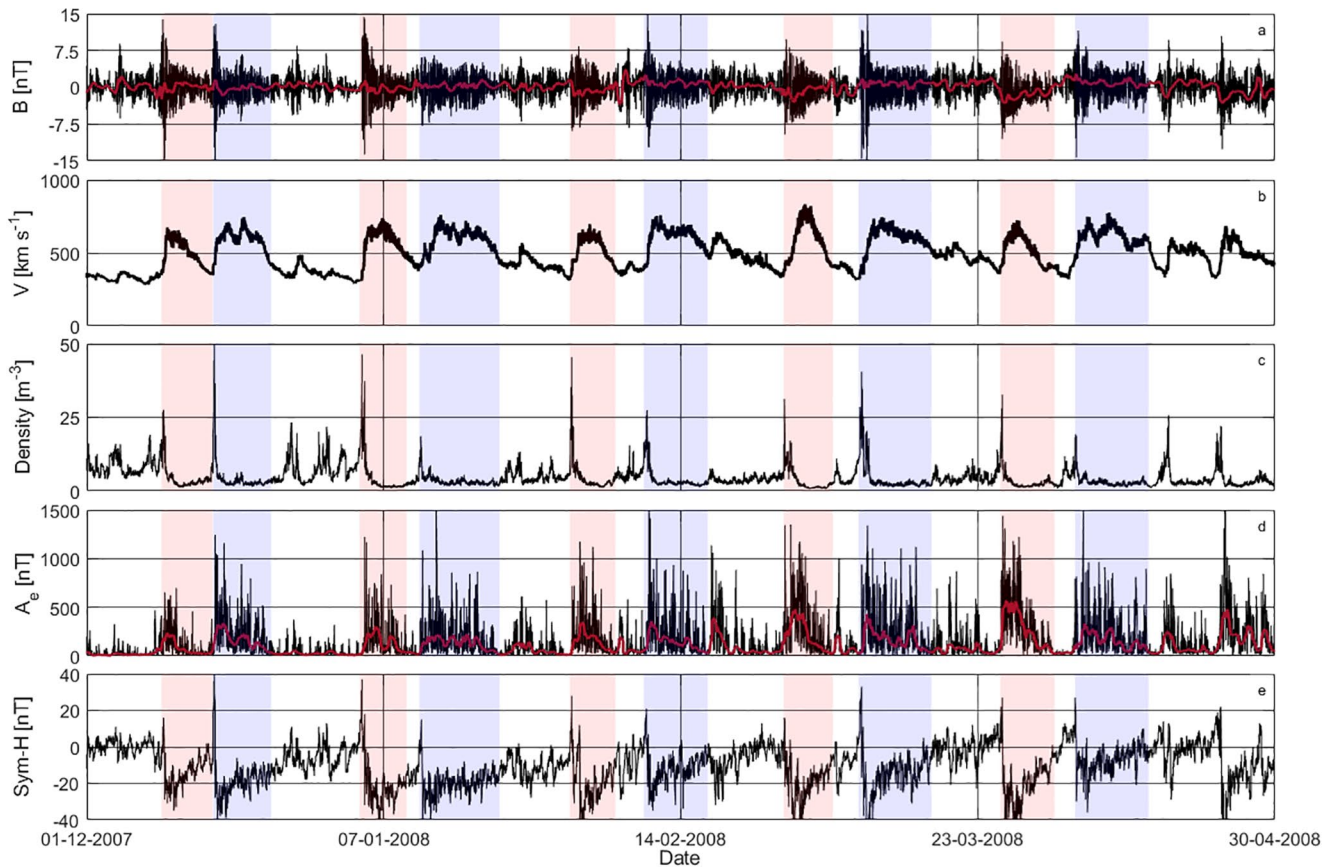


Figure 3. Solar wind and geomagnetic indices for the same time period as that shown in Figure 1: (a) solar wind magnetic field B_2 component, (b) solar wind speed along the x -axis, (c) AE index, and (d) SYM-H index.

(periods of 24, 12, 8, 6, etc hours). While both these are impacted by geomagnetic activity, the main ionospheric response is located at low frequency, where spectral peaks are observed with periods of approximately $P_1 = 27$, $P_2 = 13.5$, $P_3 = 9$, and $P_4 = 6.75$ days.

Equivalent and related spectral features can be observed in the spectra characterizing the solar wind and geomagnetic indices, as can be seen in Figure 5. The spectral features, in this case, are the direct results of the presence of periodic CIR/HSS structures, and their magnetospheric impact. Additionally, while the solar wind is a complex system, it is not subject to multiple types of forcings in the same manner as the thermosphere-ionosphere, allowing for the spectral peaks at P_1 , P_2 , P_3 , and P_4 to have a higher signal-to-noise ratio and a lower spectral width.

The causal link between periodic HSS/CIR events, associated geomagnetic storms (shown in Figure 5), and the periodic ionospheric response (shown in Figure 4) is well established. Characterized by periods P_{1-4} , it is superimposed onto the background variability of the thermosphere-ionosphere, created by solar irradiance, normal geomagnetic activity, and GWs. A specific storm can be the main source of energy and momentum at some locations, for time intervals from several hours to at most a few days. Since the data set we used has a length of 5 months, it is expected that, while significant, the periodicities induced by HSS/CIRs won't be dominant, and the specific response at a given ionosonde location may be affected by local phenomena. In order to highlight the global ionospheric response to HSS/CIRs while minimizing the impact of local conditions, the hmF_2 and NmF_2 spectra at each location are normalized to 1. Figure 4 exemplifies this procedure for a single station, highlighting the presence of spectral peaks while minimizing the impact of the spectral background, which may vary depending on location. Combining the results from all available stations in a

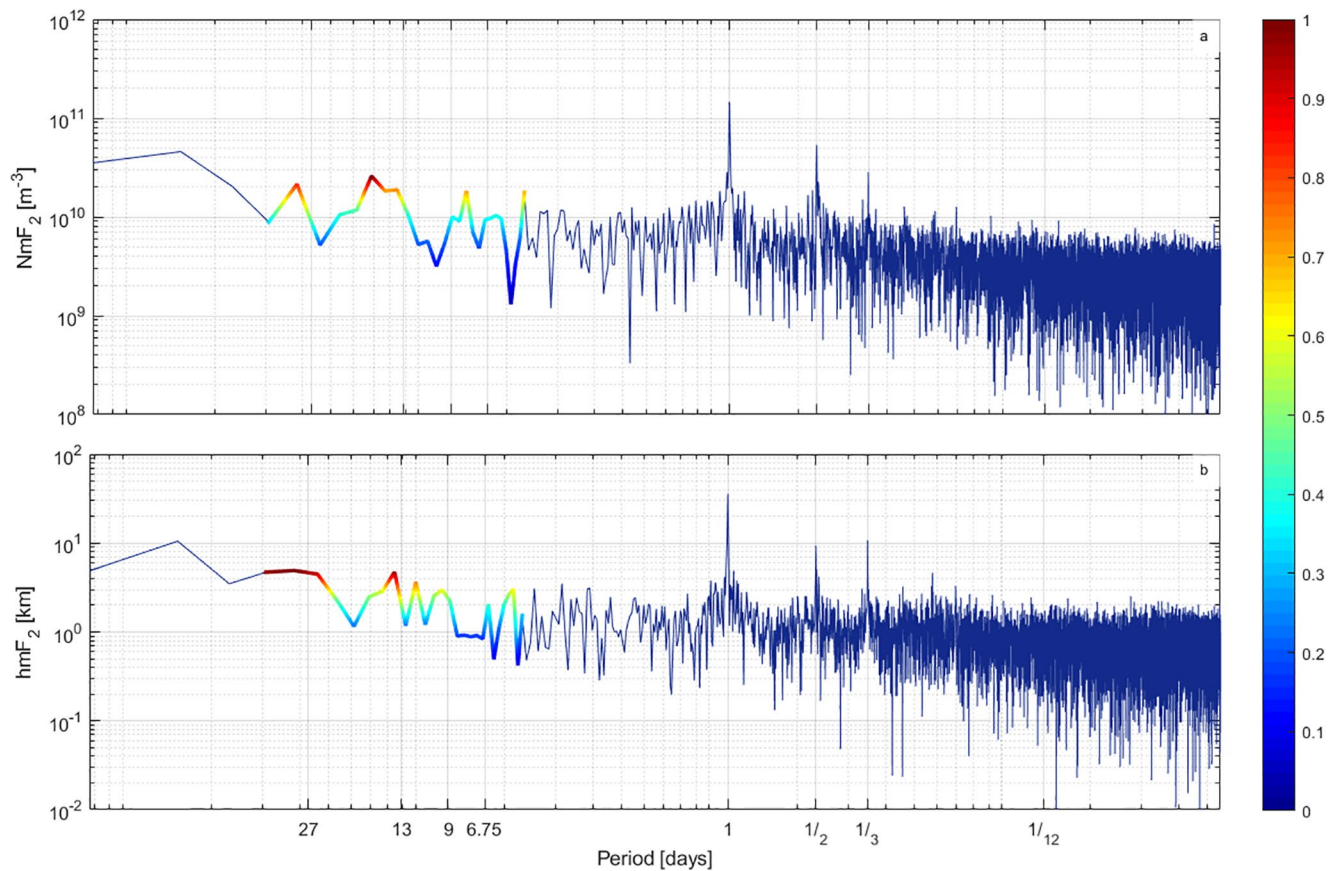


Figure 4. Sample spectra for the Millstone Hill ionosonde, showing the (a) NmF₂ and (b) hmF₂ spectrum. The low-frequency portion of the spectrum is color-coded according to a normalization performed on the period interval 5–36 days.

mixed line-color plot yields a pseudo-2-D plot (Figure 6), describing the ionospheric response as a function of period and latitude. Additionally, stations from specific latitude sectors are grouped together.

3. Results and Discussion

The hmF₂ and NmF₂ spectra depicted in Figure 6 contain peaks causally linked to those observed in the solar wind and magnetospheric spectra in Figure 5. The sequence of HSS/CIR events in the solar wind creates a magnetospheric response with the same dominant periodicities of 27, 13.5, 9, and 6.75 days, generated by the Sun's rotation period, as well as the width and separation of coronal holes (Lei, Thayer, Wang, & McPherron, 2011). By contrast, the ionospheric response is characterized by a much more complex structure. While spectral peaks with periods $P = P_{1-4}$ are present at the majority of locations, secondary peaks are identified with intermediary periods, in the intervals 15–21, 10–12, and 7–8 days. Additional peaks are identified at smaller periods for a reduced number of locations, and will not be the focus of this study. The likely cause for these additional periodicities is the non-linear nature of the energy and momentum transfer mechanisms associated with geomagnetic storms, manifested in the spectral domain by shifting a portion of the power contained in the solar wind and magnetospheric spectra to the secondary spectral peaks observed in the ionospheric spectra.

In the time domain, this may manifest in a number of ways:

1. The ionospheric response to specific storms may be different depending on geographic location, with differences in the start time and duration of the observed perturbations, as can be seen in Figures 1 and 2 and

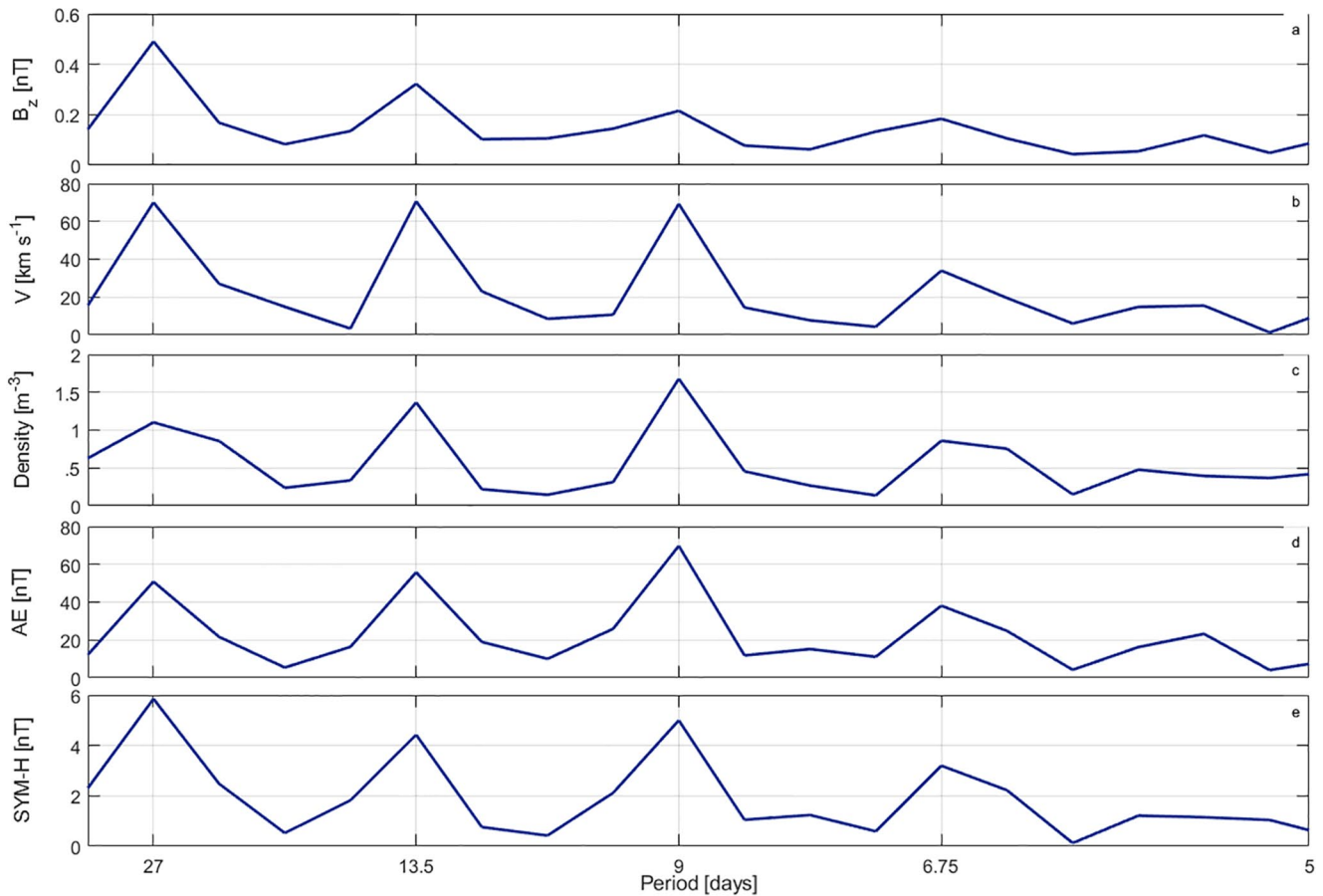


Figure 5. Same as Figure 3, but for the solar wind parameters and geomagnetic indices.

2. at a given location the response to successive storms may exhibit different delays or durations, resulting in a slightly different spectral response
3. the hmF₂ storm response has a more pulse-like response, similar to the structures observed in the solar wind and the associated geomagnetic responses (Figure 3), while in general the NmF₂ response is more complex, with a positive and negative storm phase

Thus, the spectral behavior of NmF₂, namely its P_{1-4} periodicities, is somewhat mingled compared to the more harmonic response of hmF₂ which closely follows the recurrence of storms triggered by the sequence of HSS/CIR interplanetary events. This effect might have an additional impact on the global ionospheric response as the two main ionospheric parameters, the altitude of the F-layer and its maximum density do not react in phase with the external forcing.

The non-linear transfer is more pronounced for NmF₂, resulting in discrepancies between the ionospheric response in NmF₂ and hmF₂. Most notably for $P = P_1$, 25 out of 28 locations show a spectral peak in hmF₂, while an equivalent peak in NmF₂ is only present at 11 locations. The overall hmF₂ response at a given location can be quantified through the use of an index, I_h , with possible integer values between 0-4, which we define as the total number of spectral peaks clearly evidenced with periods equal to P_{1-4} at each location, regardless of their relative or absolute amplitude. More exactly, for a given ionosonde, $I_h = \text{sum}(I_{hi})$, with $I_{hi} = 1$ if a spectral peak is observed at P_i , or 0 otherwise. Equivalently for NmF₂, we define the I_N index. The values for each station are listed in Table 2. Since $I_h > I_N$ for 22 locations, the non-linear nature of the solar wind-magnetosphere-ionosphere coupling has a much greater impact on the plasma density in the F-layer, rather than on the altitude of the layer itself. This result is observed particularly in the additional spectral peaks in Figure 6b.

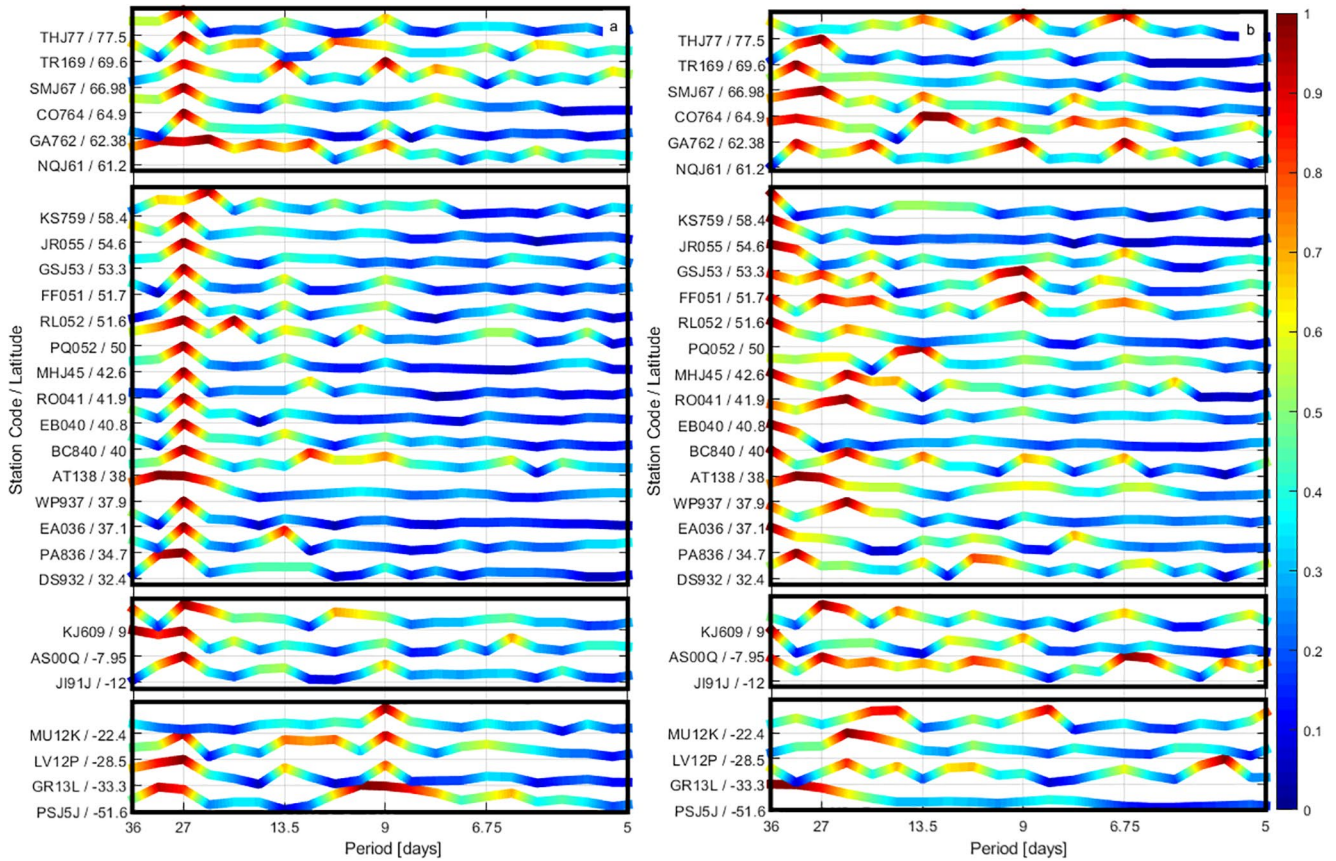


Figure 6. Pseudo 2-D plot showing the low-frequency amplitude spectra as a function of latitude for (a) hmF_2 and (b) NmF_2 . Each line represents the normalized amplitude spectrum for a different ionosonde station, additionally color-coded to highlight spectral features present at multiple locations. The stations are grouped into four categories: high latitude, northern hemisphere mid-latitude, low-latitude, and southern hemisphere mid-latitude; with each group encased in a rectangle.

The mean value of I_N has a significant latitude dependence, with $\overline{I_N} = 2.3$ at high-latitude, 2.2 at mid-latitude in the northern hemisphere, and only 1.6 at low-latitudes. Additionally, a seasonal effect may also influence the ionospheric storm response, since $\overline{I_N} = 1.25$ in the southern hemisphere mid-latitudes. By contrast, $\overline{I_h} = 2.8$ at high latitudes, increasing to 3.3 at low latitudes and 3.5 in the southern hemisphere. Additional investigation is required to clarify these effects, either using measurements from more locations, covering a wider time interval, or involving additional data types. One interesting feature to note is that the values of I_N are smaller than 4 at all locations, indicating that some or all of the dominant spectral peaks are shifted in the NmF_2 spectra, relative to the spectral peaks observed in the solar wind and geomagnetic indices.

To further investigate the correlation between the low-frequency response of the ionosphere to the recurrent sequence of interplanetary events, mediated by magnetospheric processes, we search for a quantitative measure of similarities between spectra of ionospheric parameters (hmF_2 and NmF_2) and spectra of the solar wind (B , B_z , and V_x) and geomagnetic measures of activity (AE and SYM-H indices). The Pearson correlation coefficient is used:

$$\rho(A, B) = \frac{1}{M-1} \sum_{i=1}^M \left(\frac{A_i - \mu_A}{\sigma_A} \right) \left(\frac{B_i - \mu_B}{\sigma_B} \right) \quad (2)$$

where M is the total number of periods $P \in [5, 36]$ days for which the spectral amplitude was determined, A and B are the two spectra for which the correlation coefficient is being determined, μ is the mean value, and σ is the standard deviation.

Table 2
List of Values for the hmF₂ and NmF₂ Indices, I_h and I_N, for Each Station, Together With Geographical Coordinates

| Station code | Latitude (°) | Longitude (°) | I _h | I _N |
|--------------|--------------|---------------|----------------|----------------|
| THJ77 | 77.5 | 290.8 | 4 | 3 |
| TR169 | 69.6 | 19.2 | 3 | 2 |
| SMJ67 | 66.98 | 309.06 | 3 | 1 |
| CO764 | 64.9 | 212 | 2 | 3 |
| GA762 | 62.38 | 215 | 3 | 3 |
| NQJ61 | 61.2 | 314.6 | 2 | 2 |
| KS759 | 58.4 | 203.6 | 1 | 2 |
| JR055 | 54.6 | 13.4 | 1 | 1 |
| GSJ53 | 53.3 | 299.7 | 3 | 3 |
| FF051 | 51.7 | 358.2 | 4 | 2 |
| RL052 | 51.6 | 358.7 | 3 | 3 |
| PQ052 | 50 | 14.5 | 3 | 1 |
| MHJ45 | 42.6 | 288.5 | 3 | 3 |
| RO041 | 41.9 | 12.5 | 2 | 2 |
| EB040 | 40.8 | 0.5 | 3 | 2 |
| BC840 | 40 | 255 | 4 | 2 |
| AT138 | 38 | 23.5 | 3 | 3 |
| WP937 | 37.9 | 284.5 | 1 | 3 |
| EA036 | 37.1 | 353.3 | 3 | 2 |
| PA836 | 34.7 | 239.4 | 2 | 2 |
| DS932 | 32.4 | 260.2 | 4 | 2 |
| KJ609 | 9 | 167.2 | 3 | 2 |
| AS00Q | -7.95 | 345.6 | 3 | 1 |
| JJ91J | -12 | 283.2 | 4 | 2 |
| MU12K | -22.4 | 30.9 | 3 | 2 |
| LV12P | -28.5 | 21.2 | 4 | 0 |
| GR13L | -33.3 | 26.5 | 4 | 2 |
| PSJ5J | -51.6 | 302.1 | 3 | 1 |

For each of the two ionospheric quantities (hmF₂ and NmF₂), and for each of the five solar wind and geomagnetic data types (B, B_z, V_x, AE, and SYM-H), 28 correlation coefficients, $\rho(A_s, B)$ are determined, one for each of the ionosonde station locations, with a 95% probability that $\rho(A_s, B)$ highlights a real correlation if $\rho(A_s, B) > 0.22$ (Bevington & Robinson, 2003; Pugh & Winslow, 1966). The resulting histograms are used to estimate the probability distributions of the correlation coefficients, as shown in Figure 7. Here, the global distribution describing all 28 locations is further detailed by highlighting the contributions of individual latitude sectors. Finally, the median for each distribution and associated standard deviation are also listed, under the assumption that a Gaussian is an accurate approximation of the real distribution. Note that in this case, unlike for I_h and I_N, the whole low-frequency spectrum (periods between 36 and 5 days) was used, not just the spectral peaks. For both NmF₂ and hmF₂ the median correlation value is positive with all OMNI parameters, indicative of the solar wind-magnetosphere-ionosphere coupling. However, the median values for all distributions describing hmF₂ were higher than those of the equivalent NmF₂ distributions. The hmF₂ data exhibit a median correlation between 0.45 to 0.65 with the solar wind and geomagnetic parameters, while the range for the NmF₂ data is only between 0.19 to 0.30. Since the associated standard deviations are similar, 0.18–0.22 for hmF₂ and 0.20–0.22 for NmF₂, it can be concluded that the hmF₂ more closely follows the geomagnetic forcing. This is likely attributed to the more linear nature of the hmF₂ response, for which the positions of the spectral peaks align with those in the solar wind and geomagnetic indices. By contrast, in the NmF₂ spectra, the position of all or some of the dominant spectral peaks is shifted, lowering the correlation coefficients.

Both the hmF₂ and NmF₂ spectra exhibit the strongest correlation with solar wind B_z and the least strong with n_p. Interestingly, of the two geomagnetic indices considered, a stronger correlation is observed with the spectral characteristics of SYM-H, suggesting that the ionospheric storm response can more strongly be attributed to penetrating electric fields in this case, rather than high-latitude Joule heating and particle precipitation. Similar conclusions have been previously reported by Verkhoglyya et al. (2013) and Vijaya Lekshmi et al. (2008) using different approaches and investigating different periods of time. Penetrating electric fields are sudden events, closely coupled to the external driver. Therefore, their ionospheric effects might be characterized by a closer similarity, in terms of

periodicities, with the driver spectral features. On the other hand, Joule heating at higher latitudes necessarily adds a time scale for the ionospheric response to the driver, linked to the particle heating itself and also to the time required for the associated ionospheric perturbation to propagate at lower latitudes. Finally, note that the subgroups of locations belonging to any given latitude interval do not display a noticeably different probability distribution function than that of the whole group of stations. This points to truly global nature of the ionospheric storm response, although further investigation is required to determine to what extent this is valid for a less impactful series of geomagnetic storms.

4. Summary and Conclusions

In this study, we used ionosonde hmF₂ and NmF₂ data (Figures 1 and 2) from 28 stations listed in Table 1, as well as solar wind measurements and geomagnetic indices taken from the OMNI data set (Figure 3) to investigate the ionospheric impact of a sequence of 10 HSS/CIR events during 2007–2008. Spectral analysis is used to highlight the low-frequency impact of this phenomena in the solar wind and geomagnetic activity

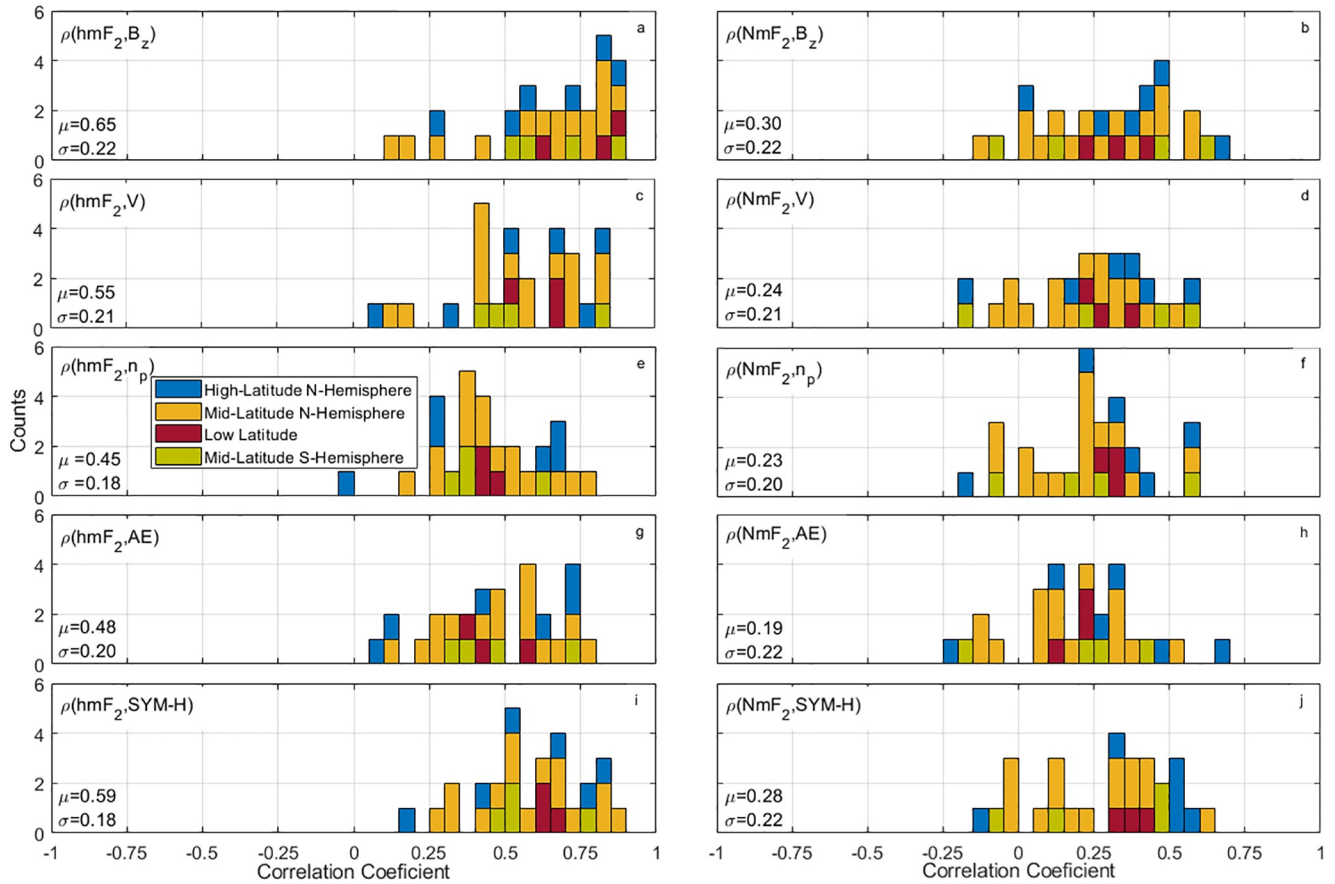


Figure 7. Histograms of the correlation coefficients between the ionospheric parameter spectra and the spectra of the solar wind and geomagnetic indices: (a) hmF₂ and B_z; (b) NmF₂ and B_z; (c) hmF₂ and V; (d) NmF₂ and V; (e) hmF₂ and n_p; (f) NmF₂ and n_p; (g) hmF₂ and AE; (h) NmF₂ and AE; (i) hmF₂ and SYM-H; (j) NmF₂ and SYM-H. Each histogram covers the entire group of 28 ionosonde stations, while the color blocks depict the contributions from the subgroups containing the locations within specific latitude ranges. For each pair of variables, the median and standard deviation are listed.

(Figure 5) and the associated ionospheric impact (Figure 4). In order to account for the different spectral backgrounds at each location, the low-frequency range (periods between 5 and 36 days) of each spectrum is normalized to 1 (Figure 4). While the solar wind and geomagnetic spectra contain local maxima at precisely $P_1 = 27$, $P_2 = 13.5$, $P_3 = 9$, and $P_4 = 6.75$ days (Figure 5), the ionospheric spectra are characterized by a more complex structure, with secondary peaks adding to or replacing the main ones, particularly for NmF₂ (Figure 6).

This increase in complexity is likely caused by the non-linear nature of the magnetosphere-ionosphere coupling. By analyzing both the NmF₂ and hmF₂ spectra, we show that this non-linearity is much more pronounced for NmF₂, and potentially latitude dependent. Two indices are introduced, I_N and I_h , counting how many peaks with periods P_1 , P_2 , P_3 , and P_4 occur at each location in the NmF₂ (I_N) and hmF₂ spectra, respectively. The results listed in Table 2 show that $I_N < I_h$ in the majority of cases, with $I_N < 4$ at all locations, meaning that no location shows all the four periodicities observed for the forcing. Additionally, the non-linearity of the ionospheric response in NmF₂ may be latitude and seasonally dependent, although future work is necessary to clarify this, involving additional measurements and data types.

The coupling of the ionospheric parameters and the solar wind data (B_z, V, and n_p) and geomagnetic indices (AE and SYM-H) is investigated quantitatively by estimating the degree of similarity between the spectral features of ionospheric height and density of the F-layer (through hmF₂ and NmF₂) and forcing (through solar wind variables B_z, V, n_p, and geomagnetic indices, AE and SYM-H). Such a quantitative measure was derived from a computation of the correlation coefficients between the spectra themselves. For each variable pair, a probability distribution function describing the level of spectral correlation is constructed using

spectra from all 28 ionosondes (Figure 7). The resulting distributions are characterized by higher median values for hmF₂, whose spectra closely follow those characterizing the sequence of HSS/CIR interplanetary events. At the same time, the NmF₂ median correlation is approximately 0.3 lower due to its more complex spectra. This indicates that the altitude of the F₂-layer and its maximum density exhibit a fundamentally different response to the external forcing.

Since in general, the storm response of NmF₂ is stronger than that of hmF₂, this result is further evidence of the nonlinear nature of the solar wind-magnetosphere-ionosphere coupling: the local maxima in the NmF₂ spectra are not located at P₁–P₄, or not only at these periods, decreasing the correlation. Finally, the ionospheric spectra are more strongly correlated with the solar wind B_z than V or the n_p, and also a stronger correlation with SYM-H than AE. This suggests that for the low-frequency ionospheric response, penetration electric fields play a more important role than the high-latitude Joule heating.

Data Availability Statement

The authors wish to thank T. W. Bullett and NOAA-NCEI for providing access to the ionosonde data necessary for this work, which is accessible at <http://ngdc.noaa.gov/ionosonde/data>.

Acknowledgments

This work is part of a project that has received funding from the European Union's Horizon 2020 research and innovation programme under the Marie Skłodowska-Curie grant agreement No. 800215, and also by the Romanian Ministry of Research through UEFIS-CDI PCCDI grant VESS (contract no. 18/2018) and National Core Program (LAPLAS 2019). Finally, the authors would like to thank the two reviewers for their suggestions and comments that helped improve the quality of our paper.

References

- Bevington, P. R., & Robinson, D. K. (2003). *Data reduction and error analysis for the physical sciences* (3rd ed.). McGraw-Hill Higher Education.
- Borries, C., Jakowski, N., & Wilken, V. (2009). Storm induced large scale TIDs observed in GPS derived TEC. *Annals of Geophysics*, 27, 1605–1612. <https://doi.org/10.5194/angeo-27-1605-2009>
- Chen, Y., Wang, W., Burns, A. G., Liu, S., Gong, J., Yue, X., et al. (2015). Ionospheric response to CIR-induced recurrent geomagnetic activity during the declining phase of solar cycle 23. *Journal of Geophysical Research: Space Physics*, 120, 1394–1418. <https://doi.org/10.1002/2014JA020657>
- Codrescu, M. V., Fuller-Rowell, T. J., & Foster, J. C. (1995). On the importance of E-field variability for Joule heating in the high-latitude thermosphere. *Geophysical Research Letters*, 22(17), 2393–2396. <https://doi.org/10.1029/95GL01909>
- Crowley, G., Reynolds, A., Thayer, J. P., Lei, J., Paxton, L. J., Christensen, A. B., et al. (2008). Periodic modulations in thermospheric composition by solar wind high speed streams. *Geophysical Research Letters*, 35, L21106. <https://doi.org/10.1029/2008GL035745>
- Echer, E., Tsurutani, B. T., Gonzalez, W. D., & Kozyra, J. U. (2011). High speed stream properties and related geomagnetic activity during the whole heliosphere interval (WHI): 20 March to 16 April 2008. *Solar Physics*, 274, 303–320. <https://doi.org/10.1007/s11207-011-9739-0>
- Emery, B. A., Richardson, I. G., Evans, D. S., Rich, F. J., & Wilson, G. R. (2011). Solar rotational periodicities and the semiannual variation in the solar wind, radiation belt, and aurora. *Solar Physics*, 274, 399–425. <https://doi.org/10.1007/s11207-011-9758-x>
- Fuller-Rowell, T. (2014). Physical characteristics and modeling of Earth's thermosphere. In J. Huba, R. Schunk, G. Khazanov (Eds.), *Modeling the Ionosphere-Thermosphere*. *Geophysical Monograph Series* (Vol. 201, pp. 13–27). AGU. <https://doi.org/10.1002/9781118704417.ch2>
- Fuller-Rowell, T. J., Codrescu, M. V., Moffett, R. J., & Quegan, S. (1994). Response of the thermosphere and ionosphere to geomagnetic storms. *Journal of Geophysical Research*, 99(A3), 3893–3914. <https://doi.org/10.1029/93JA02015>
- Gibson, S. E., de Toma, G., Emery, B., Riley, P., Zhao, L., Elsworth, Y., et al. (2011). The whole heliosphere interval in the context of a long and structured solar minimum: An overview from Sun to Earth. *Solar Physics*, 274, 5–27. <https://doi.org/10.1007/s11207-011-9921-4>
- Gibson, S. E., Kozyra, J. U., de Toma, G., Emery, B. A., Onsager, T., & Thompson, B. J. (2009). If the Sun is so quiet, why is the Earth ringing? A comparison of two solar minimum intervals. *Journal of Geophysical Research*, 114, A09105. <https://doi.org/10.1029/2009JA014342>
- Grandin, M., Aikio, A. T., Kozlovsky, A., Ulich, T., & Raita, T. (2015). Effects of solar wind high-speed streams on the high-latitude ionosphere: Superposed epoch study. *Journal of Geophysical Research: Space Physics*, 120, 10669–10687. <https://doi.org/10.1002/2015JA021785>
- Guo, J., Feng, X., Pulkkinen, T. I., Tanskanen, E. I., Xu, W., Lei, J., & Emery, B. A. (2012). Auroral electrojets variations caused by recurrent high-speed solar wind streams during the extreme solar minimum of 2008. *Journal of Geophysical Research*, 117, A04307. <https://doi.org/10.1029/2011JA017458>
- Katsavrias, C., Preka-Papadema, P., & Moussas, X. (2012). Wavelet analysis on solar wind parameters and geomagnetic indices. *Solar Physics*, 280, 623–640. <https://doi.org/10.1007/s11207-012-0078-6>
- King, J. H., & Papitashvili, N. E. (2005). Solar wind spatial scales in and comparisons of hourly wind and ACE plasma and magnetic field data. *Journal of Geophysical Research*, 110, A02104. <https://doi.org/10.1029/2004JA010649>
- Klenzing, J., Burrell, A. G., Heelis, R. A., Huba, J. D., Pfaff, R., & Simões, F. (2013). Exploring the role of ionospheric drivers during the extreme solar minimum of 2008. *Annals of Geophysics*, 31, 2147–2156. <https://doi.org/10.5194/angeo-31-2147-2013>
- Lei, J., Thayer, J. P., Forbes, J. M., Wu, Q., She, C., Wan, W., & Wang, W. (2008). Ionosphere response to solar wind high-speed streams. *Geophysical Research Letters*, 35, L19105. <https://doi.org/10.1029/2008GL035208>
- Lei, J., Thayer, J. P., Wang, W., & McPherron, R. L. (2011). Impact of CIR storms on thermosphere density variability during the solar minimum of 2008. *Solar Physics*, 274, 427–437. <https://doi.org/10.1007/s11207-010-9563-y>
- Lomb, N. R. (1976). Least-squares frequency analysis of unequally spaced data. *Astrophysics and Space Science*, 39(2), 447–462. <https://doi.org/10.1007/BF00648343>
- Maris, G., & Maris, O. (2009). WHI high-speed streams at geospace. *Proceeding of IAU*, 5(H15), 494–497. <https://doi.org/10.1017/S1743921310010379>
- Matamba, T. M., Habarulema, J. B., & McKinnell, L.-A. (2015). Statistical analysis of the ionospheric response during geomagnetic storm conditions over South Africa using ionosonde and GPS data. *Space Weather*, 13, 536–547. <https://doi.org/10.1002/2015SW001218>

- McGrathagan, R., Knipp, D. J., McPherron, R. L., & Hunt, L. A. (2014). Impact of equinoctial high-speed stream structures on thermospheric responses. *Space Weather*, *12*, 277–297. <https://doi.org/10.1002/2014SW001045>
- McNamara, L. F. (2006). Quality figures and error bars for autoscaled Digisonde vertical incidence ionograms. *Radio Science*, *41*, RS4011. <https://doi.org/10.1029/2005RS003440>
- Munteanu, C., Hamada, A., & Mursula, K. (2019). High-speed solar wind streams in 2007–2008: Turning on the Russell-McPherron effect. *Journal of Geophysical Research: Space Physics*, *124*, 8913–8927. <https://doi.org/10.1029/2019JA026846>
- Munteanu, C., Negrea, C., Echim, M., & Mursula, K. (2016). Effect of data gaps: Comparison of different spectral analysis methods. *Annals of Geophysics*, *34*, 437–449. <https://doi.org/10.5194/angeo-34-437-2016>
- Negrea, C., Zabolin, N., & Bullett, T. (2018). Seasonal variability of the midlatitude traveling ionospheric disturbances from Wallops Island, VA, Dynasonde data: Evidence of a semiannual variation. *Journal of Geophysical Research: Space Physics*, *123*, 5047–5054. <https://doi.org/10.1029/2017JA025164>
- Negrea, C., Zabolin, N., Bullett, T., Fuller-Rowell, T., Fang, T. W., & Codrescu, M. (2016). Characteristics of acoustic gravity waves obtained from Dynasonde data. *Journal of Geophysical Research: Space Physics*, *121*, 3665–3680. <https://doi.org/10.1002/2016JA022495>
- Pedatella, N. M., Lei, J., Thayer, J. P., & Forbes, J. M. (2010). Ionosphere response to recurrent geomagnetic activity: Local time dependency. *Journal of Geophysical Research*, *115*, A02301. <https://doi.org/10.1029/2009JA014712>
- Pugh, E. M., & Winslow, G. H. (1966). *The analysis of physical measurements*. Addison Wesley.
- Rishbeth, H., & Garriott, O. K. (1969). *Introduction to Ionospheric Physics*. International Geophysics Series (Vol. 14, p. 331). Academic Press.
- Russell, C. T., & McPherron, R. L. (1973). Semiannual variation of geomagnetic activity. *Journal of Geophysical Research*, *78*, 92–108. <https://doi.org/10.1029/JA078i001p00092>
- Scargle, J. D. (1982). Studies in astronomical time series analysis. II. Statistical aspects of spectral analysis of unevenly spaced data. *The Astrophysical Journal*, *263*, 835–853. <https://doi.org/10.1086/160554>
- Thompson, B. J., Gibson, S. E., Schroeder, P. C., Webb, D. F., Arge, C. N., Bisi, M. M., et al. (2011). A snapshot of the Sun near solar minimum: The whole heliosphere interval. *Solar Physics*, *274*, 29–56. <https://doi.org/10.1007/s11207-011-9891-6>
- Tulasi Ram, S., Lei, J., Su, S.-Y., Liu, C. H., Lin, C. H., & Chen, W. S. (2010). Dayside ionospheric response to recurrent geomagnetic activity during the extreme solar minimum of 2008. *Geophysical Research Letters*, *37*, L02101. <https://doi.org/10.1029/2009GL041038>
- Tulasi Ram, S., Liu, C. H., & Su, S.-Y. (2010). Periodic solar wind forcing due to recurrent coronal holes during 1996–2009 and its impact on Earth's geomagnetic and ionospheric properties during the extreme solar minimum. *Journal of Geophysical Research*, *115*, A12340. <https://doi.org/10.1029/2010JA015800>
- Verkhoglyadova, O. P., Tsurutani, B. T., Mannucci, A. J., Mlynczak, M. G., Hunt, L. A., Komjathy, A., & Runge, T. (2011). Ionospheric VTEC and thermospheric infrared emission dynamics during corotating interaction region and high-speed stream intervals at solar minimum: 25 March to 26 April 2008. *Journal of Geophysical Research*, *116*, A09325. <https://doi.org/10.1029/2011JA016604>
- Verkhoglyadova, O. P., Tsurutani, B. T., Mannucci, A. J., Mlynczak, M. G., Hunt, L. A., & Runge, T. (2013). Variability of ionospheric TEC during solar and geomagnetic minima (2008 and 2009): External high speed stream drivers. *Annals of Geophysics*, *31*, 263–276. <https://doi.org/10.5194/angeo-31-263-2013>
- Vijaya Lekshmi, D., Balan, N., Vaidyan, V. K., Alleyne, H., & Bailey, G. J. (2008). Response of the ionosphere to super geomagnetic storms: Observations and modeling. *Advances in Space Research*, *41*(4), 548–555. <https://doi.org/10.1016/j.asr.2007.08.029>
- Wang, W., Lei, J., Burns, A. G., Qian, L., Solomon, S. C., Wiltberger, M., & Xu, J. (2011). Ionospheric day-to-day variability around the whole heliosphere interval in 2008. *Solar Physics*, *274*, 457–472. <https://doi.org/10.1007/s11207-011-9747-0>
- Webb, D. F., Cremades, H., Sterling, A. C., Mandrini, C. H., Dasso, S., Gibson, S. E., et al. (2011). The global context of solar activity during the whole heliosphere interval campaign. *Solar Physics*, *274*, 57–86. <https://doi.org/10.1007/s11207-011-9787-5>
- Xu, J., Wang, W., Zhang, S., Liu, X., & Yuan, W. (2015). Multiday thermospheric density oscillations associated with variations in solar radiation and geomagnetic activity. *Journal of Geophysical Research: Space Physics*, *120*, 3829–3846. <https://doi.org/10.1002/2014JA020830>